International Journal of Heat and Fluid Flow 30 (2009) 514–524

Contents lists available at ScienceDirect

International Journal of Heat and Fluid Flow

journal homepage: www.elsevier.com/locate/ijhff

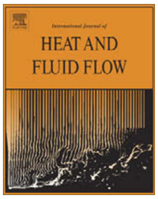

DNS of turbulent heat transfer in a channel flow with a high spatial resolution

Makoto Kozuka, Yohji Seki, Hiroshi Kawamura *

Department of Mechanical Engineering, Tokyo University of Science, Noda-shi, Chiba 278-8510, Japan

ARTICLE INFO

Article history:
Received 7 October 2008
Received in revised form 23 February 2009
Accepted 25 February 2009
Available online 18 April 2009

Keywords:
Direct numerical simulation
Turbulent heat transfer
Channel flow
Reynolds- and Prandtl-number dependence

ABSTRACT

Direct numerical simulations of turbulent heat transfer in a channel flow are performed to investigate the effects of Reynolds and Prandtl numbers on higher-order turbulence statistics such as a turbulent Prandtl number and the budget for the dissipation rate of the temperature variance. The Reynolds numbers based on the friction velocity and the channel half width are 180 and 395, and the molecular Prandtl numbers *Pr*'s 0.71–10.0. Careful attention is paid to ensure accuracy of the higher-order statistics through the use of a high spatial resolution comparable to Batchelor length scale. The wall-asymptotic value of the turbulent Prandtl number is mostly independent of Reynolds number for the current range of *Pr*'s. The budget for the dissipation rate of the temperature variance has been computed, and the negligible effect of a Reynolds number on the sum of all source and sink terms in near-wall region in the current computational range is found. This result is quite similar to the one in the budget for the dissipation rate of turbulent energy. In addition, a priori test for existing models is also performed to assess the *Pr* dependence on the individual terms and their summations in the budget.

1. Introduction

Passive scalar transport in turbulent wall flows is of great importance in many engineering applications involving heat and mass transfer, turbulent mixing and combustion. In practical calculations, various turbulence models are widely used in software for computational fluid dynamics and heat transfer.

Direct numerical simulations (DNS) has become a valuable tool for the analysis of turbulent heat transfer and has been offering a theoretical basis on turbulence statistics for different Reynolds and Prandtl numbers. Kim and Moin (1989) performed monumental DNS of the turbulent channel flow with a passive scalar for Reynolds number $Re_\tau = 180$ at Prandtl number of $Pr = 0.10$, 0.71 and 2.0 using uniform volumetric heating condition, where Re_τ is based on the friction velocity u_τ and the channel half width δ. Several researchers have since devoted growing computational power to higher Reynolds and Prandtl numbers (e.g., Lyons et al., 1991; Kasagi et al., 1992). The current group of authors (e.g., Kawamura et al., 1999; Abe and Kawamura, 2002; Abe et al., 2004) executed DNS for higher Re_τ up to 1020 with $Pr = 0.025$ and 0.71. Na and Hanratty (2000) and Tiselj et al. (2001) simulated turbulent channel flow for moderate *Pr*'s (≈ 10.0) with low Re_τ of $Re_\tau = 150$ and 180. In these previous studies, the majority of the effort was expended on Re_τ and Pr dependencies of lower-order turbulence statistics and characteristic turbulent structures. Higher-order statistics, such as the budget for the dissipation rate of temperature variance, were also obtained, but adequate attention has not been paid to numerical accuracy. The spatial resolutions were often set so as to be much coarser in comparison with Batchelor length scale η_θ, which is estimated as $\eta_\theta = \eta \cdot Pr^{-1/2}$, where η is Kolmogorov length scale. As η_θ becomes finer with increasing *Pr*, a fine spatial resolution must be employed to obtain reliable higher-order turbulence statistics on performing DNS for high *Pr*.

In the current paper, a series of DNS has been carried out for moderate Reynolds and Prandtl numbers using a high spatial resolution. The calculated range is $Re_\tau = 180$–395 at $Pr = 0.71$–10.0, as given in Table 1. Various turbulence statistics, including higher-order ones associated with fully developed scalar fields, are presented and discussed with emphasis on the effects of Re_τ and *Pr*. The range of newly obtained data in this work is summarized in Table 2. Budgets for the dissipation rate of the temperature variance and of the turbulent heat flux are first obtained for various *Pr*'s in the current study. The accuracy of these higher-order statistics is examined below through the use of pre-multiplied energy spectra.

2. Numerical procedures

The configuration used is a fully developed turbulent channel flow as shown in Fig. 1. The flow is driven by a uniform pressure gradient. The temperature field is imposed by uniform heating over both walls with a constant time-averaged heat flux. Note that in the current thermal boundary condition, the statistically averaged heat flux is constant, but the instantaneous one is time dependent.

---

* Corresponding author. Present address: Department of System Engineering, Tokyo University of Science, Suwa, Chino-shi, Nagano 391-0292, Japan

E-mail addresses: kozuka.makoto@gmail.com (M. Kozuka), kawa@rs.noda.tus.ac.jp (H. Kawamura).

0142-727X/$ - see front matter © 2009 Published by Elsevier Inc.
doi:10.1016/j.ijheatfluidflow.2009.02.023

Table 1
Computational condition.

	Case 1	Case 2	Case 3
$Re_\tau\ (= u_\tau \cdot \delta/\nu)$	180	180	395
$Re_b\ (= u_b \cdot 2\delta/\nu)$	5700	5700	14000
Pr	0.71, 1, 2,10	7, 10	0.71,1, 2, 5, 7, 10
Computational volume	$6.4\delta \times 2\delta \times 3.2\delta$	$6.4\delta \times 2\delta \times 3.2\delta$	$6.4\delta \times 2\delta \times 3.2\delta$
Grid number	$1024 \times 480 \times 512$	$2048 \times 480 \times 512$	$2048 \times 480 \times 512$
Spatial Resolution (Δx^+)	1.13	0.563	1.23
Spatial Resolution (Δy^+)	0.0504–0.972	0.0504–0.972	$0.111 \cdot 2.13$
Spatial resolution (Δz^+)	1.13	1.13	2.47

Table 2
Obtained data in the current study. Reynolds numbers are $Re_\tau = 180$ and 395 in this study. k_θ and ε_θ are the temperature variance and its dissipation rate. $\varepsilon_{1\theta}$ and $\varepsilon_{2\theta}$ denotes the dissipation rates of the streamwise and wall normal turbulent heat flux, respectively (see Sections 3 and 4).

Pr	0.71	1.0	2.0	5.0	7.0	10.0
Budget for k_θ		Existing				
Budget for ε_θ	Existing	New[a]				New[b]
Budget for $\varepsilon_{1\theta}$		New[a]				New[b]
Budget for $\varepsilon_{2\theta}$		New[a]				New[b]

[a] Firstly obtained with a high accuracy.
[b] Firstly obtained with a tolerable accuracy.

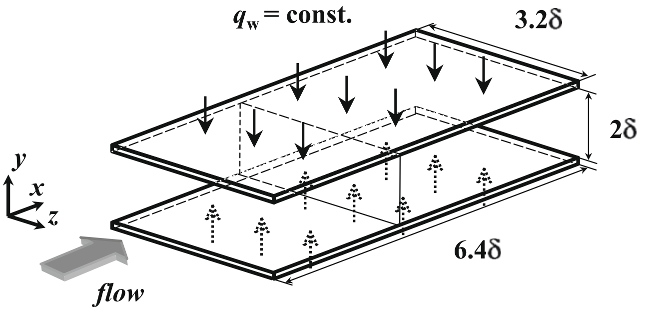

Fig. 1. Configuration of the computational domain.

The periodic boundary conditions are imposed in the streamwise (x) and spanwise (z) directions. The walls are non-slip. A uniform grid mesh is used in the horizontal direction, and a non-uniform one in the wall-normal (y) direction. All fluid properties are treated as constant.

The governing equations are incompressible continuity, Navier–Stokes, and energy equations:

$$\frac{\partial u_i^+}{\partial x_i^*} = 0, \tag{1}$$

$$\frac{\partial u_i^+}{\partial t^*} + u_j^+ \frac{\partial u_i^+}{\partial x_j^*} = -\frac{\partial p'^+}{\partial x_i^*} + \frac{1}{Re_\tau} \frac{\partial^2 u_i^+}{\partial x_j^* \partial x_j^*} - \frac{\partial \bar{p}^+}{\partial x_1^*} \delta_{i1}, \tag{2}$$

$$\frac{\partial \theta^+}{\partial t^*} + u_j^+ \frac{\partial \theta^+}{\partial x_j^*} = \frac{1}{Re_\tau \cdot Pr} \frac{\partial^2 \theta^+}{\partial x_j^* \partial x_j^*} + \frac{u_1^+}{\langle \bar{u}_1^+ \rangle}. \tag{3}$$

Here, δ_{i1} is Kronecker delta, and $i = 1, 2, 3$ indicate x, y and z directions, respectively. The variables u, t and p denote velocity, time, and pressure. Transformed temperature $\theta (= T_w - T)$ is introduced to be satisfied with the constant heat-flux boundary condition, where T_w is the temperature at the wall. The angular bracket represents integration over the channel cross-section. The overbar denotes averaging with respect to time and space. The quantities shown in superscript (+) indicate those normalized by u_τ and $T_\tau (= Q_w/\rho c_p u_\tau)$ and in superscript $(*)$, those normalized by δ, where Q_w, ρ, c_p are given averaged surface heat flux, density, and specific heat at constant pressure, respectively.

The fractional step method is adopted for the coupling between continuity and Navier–Stokes equations. The second-order Crank–Nicolson scheme and the Adams–Bashforth scheme are employed as the time-advance algorithms: the former for the vertical viscous term, the latter for the other viscous and convection terms. For spatial discretization, the finite difference method is used: the fourth-order central scheme is employed for the x and z directions and the second-order one for the y direction. Further details of the numerical procedures can be found in Kawamura et al. (1998, 2000).

Computational conditions, such as the box size, the grid number, and the spatial resolution, are given in Table 1. The spaces in the x and z directions are $\Delta x^+ = 0.56–1.2$ and $\Delta z^+ = 1.1–2.5$, which correspond to $\Delta x/\eta_\theta < 1$ and $\Delta z/\eta_\theta < 2$ at the channel center, respectively. The spaces in the y direction will be discussed later by comparison with η and η_θ for the current Re_τ's and Pr's over the channel cross-section.

3. Transport equation for dissipation rate of temperature variance

The transport equation for the dissipation rate $\varepsilon_\theta\ (= \kappa \overline{(\partial \theta'/\partial x_k)^2})$ of the temperature variance $k_\theta\ (= \overline{\theta'\theta'}/2)$ is given as:

$$\frac{D\varepsilon_\theta^+}{Dt^+} = P_{\varepsilon_\theta}^{(1)} + P_{\varepsilon_\theta}^{(2)} + P_{\varepsilon_\theta}^{(3)} + P_{\varepsilon_\theta}^{(4)} + T_{\varepsilon_\theta} + V_{\varepsilon_\theta} - \gamma_{\varepsilon_\theta}. \tag{4}$$

Production by mean temperature gradient:

$$P_{\varepsilon_\theta}^{(1)} = -\frac{2}{Pr} \overline{\frac{\partial u_j'^+}{\partial x_k^+} \frac{\partial \theta'^+}{\partial x_k^+}} \frac{\partial \bar{\theta}^+}{\partial x_j^+}. \tag{5}$$

Production by mean velocity gradient:

$$P_{\varepsilon_\theta}^{(2)} = -\frac{2}{Pr} \overline{\frac{\partial \theta'^+}{\partial x_j^+} \frac{\partial \theta'^+}{\partial x_k^+}} \frac{\partial \bar{u}_j^+}{\partial x_k^+}. \tag{6}$$

Gradient production:

$$P_{\varepsilon_\theta}^{(3)} = -\frac{2}{Pr} \overline{u_j'^+ \frac{\partial \theta'^+}{\partial x_k^+}} \frac{\partial^2 \bar{\theta}^+}{\partial x_j^+ \partial x_k^+}. \tag{7}$$

Turbulent production:

$$P_{\varepsilon_\theta}^{(4)} = -\frac{2}{Pr} \overline{\frac{\partial u_j'^+}{\partial x_k^+} \frac{\partial \theta'^+}{\partial x_k^+} \frac{\partial \theta'^+}{\partial x_j^+}}. \tag{8}$$

Turbulent diffusion:

$$T_{\varepsilon_\theta} = -\frac{1}{Pr} \frac{\partial}{\partial x_j^+} \left(\overline{u_j'^+ \frac{\partial \theta'^+}{\partial x_k^+} \frac{\partial \theta'^+}{\partial x_k^+}} \right). \tag{9}$$

Viscous diffusion:

$$V_{\varepsilon_\theta} = \frac{1}{Pr^2}\frac{\partial^2}{\partial x_j^{+2}}\left(\overline{\frac{\partial\theta'^+}{\partial x_k^+}\frac{\partial\theta'^+}{\partial x_k^+}}\right). \tag{10}$$

Dissipation:

$$\gamma_{\varepsilon_\theta} = \frac{2}{Pr^2}\overline{\left(\frac{\partial^2\theta\prime^+}{\partial x_k^+\partial x_j^+}\right)^2}, \tag{11}$$

where κ denotes the thermal diffusivity. The transport equation is normalized by the wall units. The effects of Re_τ and Pr on the individual terms and their sums in ε_θ-budget are discussed in Section 5.5. Assessments of existing models in the ε_θ equation are also reported in that section.

4. Transport equations for turbulent heat flux and its dissipation rate

The following are the transport equations for turbulent heat flux $\overline{u_i'\theta'}$ and its dissipation rate $\varepsilon_{i\theta}$. The budgets can be derived from the Navier–Stokes and the energy equations. The transport equation for $\overline{u_i'\theta'}$ is as shown below:

$$\frac{D\overline{u_i'^+\theta'+}}{Dt^+} = P_{i\theta} + T_{i\theta} + V_{i\theta} + \psi_{i\theta} - \varepsilon_{i\theta}. \tag{12}$$

Production:

$$P_{i\theta} = -\overline{u_i'^+u_k'^+}\frac{\partial\overline{\theta}^+}{\partial x_k^+} - \overline{u_k'^+\theta'^+}\frac{\partial\overline{u}_i^+}{\partial x_k^+}. \tag{13}$$

Turbulent diffusion:

$$T_{i\theta} = -\frac{\partial}{\partial x_k^+}\left(\overline{u_i'^+u_k'^+\theta'^+}\right). \tag{14}$$

Viscous diffusion:

$$V_{i\theta} = \frac{\partial}{\partial x_k^+}\left(\overline{\theta'^+\frac{\partial u_i'^+}{\partial x_k^+}} + \frac{1}{Pr}\overline{u_i'^+\frac{\partial\theta'^+}{\partial x_k^+}}\right). \tag{15}$$

Temperature pressure gradient correlation:

$$\psi_{i\theta} = -\overline{\theta'^+\frac{\partial p'^+}{\partial x_i^+}}. \tag{16}$$

Dissipation:

$$\varepsilon_{i\theta} = \left(1+\frac{1}{Pr}\right)\overline{\frac{\partial u_i'^+}{\partial x_k^+}\frac{\partial\theta'^+}{\partial x_k^+}}. \tag{17}$$

The transport equation for $\varepsilon_{i\theta}$ is;

$$\frac{D\varepsilon_{i\theta}^+}{Dt^+} = P_{\varepsilon_{i\theta}}^{(1)} + P_{\varepsilon_{i\theta}}^{(2)} + P_{\varepsilon_{i\theta}}^{(3)} + P_{\varepsilon_{i\theta}}^{(4)} + T_{\varepsilon_{i\theta}} + D_{\varepsilon_{i\theta}} + \psi_{\varepsilon_{i\theta}} - \gamma_{\varepsilon_{i\theta}}. \tag{18}$$

Production by mean temperature gradient:

$$P_{\varepsilon_{i\theta}}^{(1)} = -\left(1+\frac{1}{Pr}\right)\overline{\frac{\partial u_i'^+}{\partial x_j^+}\frac{\partial u_k'^+}{\partial x_j^+}}\frac{\partial\overline{\theta}^+}{\partial x_k^+}. \tag{19}$$

Production by mean velocity gradient:

$$\begin{aligned} P_{\varepsilon_{i\theta}}^{(2)} = &-\left(1+\frac{1}{Pr}\right)\overline{\frac{\partial u_k'^+}{\partial x_j^+}\frac{\partial\theta'^+}{\partial x_j^+}}\frac{\partial\overline{u}_i^+}{\partial x_k^+} \\ &-\left(1+\frac{1}{Pr}\right)\left(\overline{\frac{\partial u_i'^+}{\partial x_k^+}\frac{\partial\theta'^+}{\partial x_j^+}} + \overline{\frac{\partial u_i'^+}{\partial x_j^+}\frac{\partial\theta'^+}{\partial x_k^+}}\right)\frac{\partial\overline{u}_k^+}{\partial x_j^+}. \end{aligned} \tag{20}$$

Gradient production:

$$P_{\varepsilon_{i\theta}}^{(3)} = -\left(1+\frac{1}{Pr}\right)\overline{u_k'^+\frac{\partial\theta'^+}{\partial x_j^+}}\frac{\partial^2\overline{u}_i^+}{\partial x_j^+\partial x_k^+} - \left(1+\frac{1}{Pr}\right)\overline{u_k'^+\frac{\partial u_i'^+}{\partial x_j^+}}\frac{\partial^2\overline{\theta}^+}{\partial x_j^+\partial x_k^+}. \tag{21}$$

Turbulent production:

$$P_{\varepsilon_{i\theta}}^{(4)} = -\left(1+\frac{1}{Pr}\right)\overline{\frac{\partial u_k'^+}{\partial x_j^+}\left(\frac{\partial u_i'^+}{\partial x_k^+}\frac{\partial\theta'^+}{\partial x_j^+} + \frac{\partial u_i'^+}{\partial x_j^+}\frac{\partial\theta'^+}{\partial x_k^+}\right)}. \tag{22}$$

Turbulent diffusion:

$$T_{\varepsilon_{i\theta}} = -\left(1+\frac{1}{Pr}\right)\frac{\partial}{\partial x_k^+}\overline{\left(u_k'^+\frac{\partial u_i'^+}{\partial x_j^+}\frac{\partial\theta'^+}{\partial x_j^+}\right)}. \tag{23}$$

Viscous diffusion:

$$V_{\varepsilon_{i\theta}} = \left(1+\frac{1}{Pr}\right)\frac{\partial}{\partial x_k^+}\left(\overline{\frac{\partial\theta'^+}{\partial x_j^+}\frac{\partial^2 u_i'^+}{\partial x_j^+\partial x_k^+}} + \frac{1}{Pr}\overline{\frac{\partial u_i'^+}{\partial x_j^+}\frac{\partial^2\theta'^+}{\partial x_j^+\partial x_k^+}}\right). \tag{24}$$

Temperature gradient correlation:

$$\psi_{\varepsilon_{i\theta}} = -\left(1+\frac{1}{Pr}\right)\overline{\frac{\partial\theta'^+}{\partial x_j^+}\frac{\partial^2 p'^+}{\partial x_i^+\partial x_j^+}}. \tag{25}$$

Dissipation:

$$\gamma_{\varepsilon_{i\theta}} = \left(1+\frac{1}{Pr}\right)^2\overline{\frac{\partial^2 u_i'^+}{\partial x_j^+\partial x_k^+}\frac{\partial^2\theta'^+}{\partial x_j^+\partial x_k^+}}. \tag{26}$$

Both equations are normalized by the wall units. The Reynolds and Prandtl number dependencies of the individual terms in $\overline{u_i'\theta'}$ and $\varepsilon_{i\theta}$ budgets are investigated in Section 5.6.

5. Results and discussion

5.1. Validation of mesh resolution

The Kolmogorov $(=(\nu^3/\varepsilon)^{1/4})$ and the Batchelor length scales $(=(\kappa^2\nu/\varepsilon^{1/4})$ are plotted in Fig. 2, where ν is the kinematic viscosity and $\varepsilon(=\nu\overline{(\partial u_i'/\partial x_k)^2})$ the average of the dissipation of the turbulent energy k. These length scales are approximately constant in the near-wall region and increase in the outer region. Near the wall, η^+ and η_θ^+ are about 1.5 and 0.50 for $Re_\tau = 180$ at $Pr = 10.0$ as seen in Fig. 2a, where the minimum grid spacing of Δy^+ equals 0.050. This indicates that the spatial resolution in the y direction is significantly finer than η^+ and η_θ^+ in the near-wall region. At the channel center, the magnitude of $\Delta y^+(\approx 1.0)$ is comparable to η_θ^+, and therefore adequate for resolving the smallest length scale for $Re_\tau = 180$ at $Pr = 0.71$—10.0 over the channel section. In the case of $Re_\tau = 395$ also, Δy^+ is much smaller than the η_θ^+ for all calculated Pr's in the near-wall region as seen in Fig. 2b. Away from the wall, Δy^+ is comparable to η_θ^+ if for $Pr = 0.71$—2.0, while larger if for $Pr = 5.0$—10.0. This point is investigated to evaluate the validation of the mesh resolution for more details in relation with the pre-multiplied energy spectra.

The pre-multiplied one-dimensional streamwise energy spectra at the channel center are plotted in Fig. 3 for $k_x^2\phi_{\theta\theta}$, $k_x^3\phi_{\theta\theta}$ and $k_x^4\phi_{\theta\theta}$ normalized by η_θ, where k_x is the wavenumber in the x direction. For homogeneous turbulence, ε_θ corresponds to $k_x^2\phi_{\theta\theta}$; and $\gamma_{\varepsilon_\theta}$, the dissipation of ε_θ (see Eq. (11)), to $k_x^4\phi_{\theta\theta}$ (Kida and Yanase, 1999). It is known that the temperature energy spectra in the viscous-diffusive subrange can be normalized by η_θ. Indeed, Fig. 3a indicates that the pre-multiplied energy spectra collapse with each other for $Re_\tau = 180$ with $Pr = 0.71$—10.0. In the case of $Re_\tau = 395$, the distributions of $k_x^2\phi_{\theta\theta}$ also show good collapse for all simulated Pr's as seen in Fig. 3b. However, a slight deviation can be seen in $k_x^3\phi_{\theta\theta}$ of $Pr = 7.0$ and 10.0 and in $k_x^4\phi_{\theta\theta}$ of $Pr = 5.0$ and 7.0. The deviations is more noticeable in $k_x^4\phi_{\theta\theta}$ for $Pr = 10.0$. These are caused by insufficient wall-normal grid spaces as discussed in the previous section. This analysis indicates that $\Delta x/\eta_\theta < 0.9$ is required for an accurate resolution of ε_θ, while $\Delta x/\eta_\theta < 0.5$ for that of $\gamma_{\varepsilon_\theta}$. According-

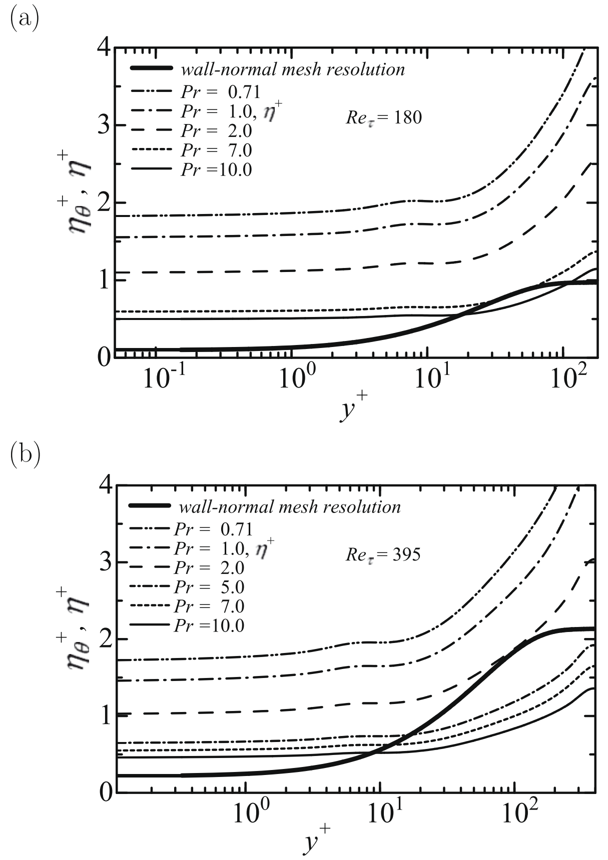

Fig. 2. Profiles of η_θ^+ and η^+: (a) $Re_\tau = 180$ and (b) $Re_\tau = 395$.

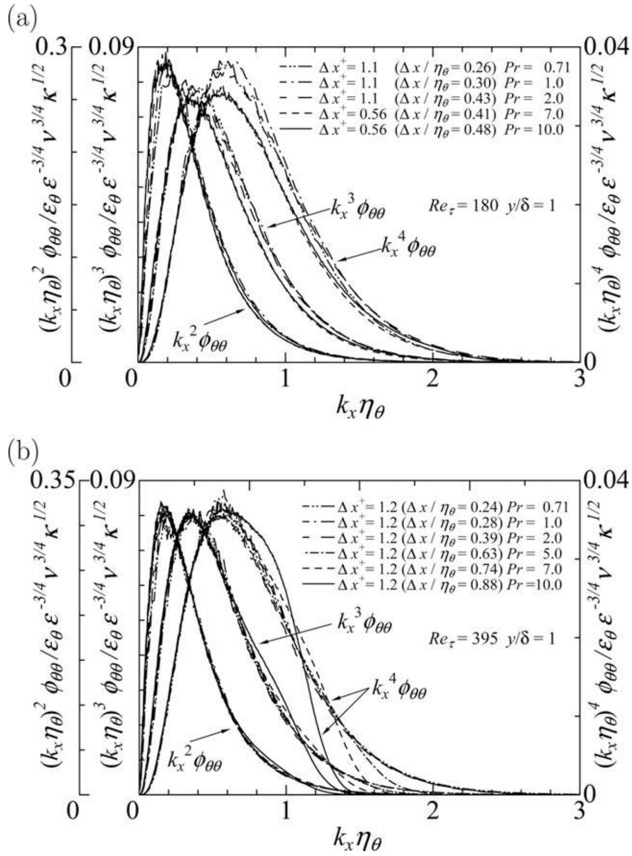

Fig. 3. Pre-multiplied one-dimensional streamwise energy spectra normalized by $\eta_\theta, t_\eta = (\nu/\varepsilon)^{1/2}$ and ε_θ at the channel center: (a) $Re_\tau = 180$ and (b) $Re_\tau = 395$.

ingly, we will discuss ε_θ itself up to $Pr = 10.0$, while its budget up to $Pr = 7.0$.

The peak of the dissipation spectra for $k_x^2\phi_{\theta\theta}$ (i.e., ε_θ) occurs at $k_x\eta_\theta \approx 0.2$ for both Re_τ's, which is in excellent agreement with Tennekes and Lumley's analysis (1972). On the other hand, the peak for $k_x^4\phi_{\theta\theta}$ (i.e., $\gamma_{\varepsilon_\theta}$) takes place at $k_x\eta_\theta \approx 0.6$. This indicates that the dominant length scales of ε_θ and $\gamma_{\varepsilon_\theta}$ are both larger than η_θ. In addition, these length scales do not depend much on Pr in the current range, although that of $\gamma_{\varepsilon_\theta}$ slightly decreases with increasing Pr (see Fig. 3a).

5.2. Mean temperature

The mean temperature is shown in Fig. 4. The current results are compared with the empirical equation proposed by Kader (1981) and existing heat transfer models: one is the zero-equation model in which the turbulent Prandtl number is derived from Kays and Crawford's equation (2004) (ZEROKC, hereafter) and another is the two-equation model by Abe et al. (1995) (TWOAKN, hereafter). In the calculations of these models, all turbulence quantities, other than $\overline{\theta}$, are obtained from current DNS data.

The prediction of Kader's equation roughly agrees with the current DNS for $Re_\tau = 395$ as shown in Fig. 4b. Strictly speaking, however, the differences in the logarithmic region are slight but increasing with increasing Pr. Note that with increasing Re_τ, the temperature at the channel center decreases if $Pr > 1.0$, while it increases if $Pr \leqslant 1.0$. This indicates that turbulence has a better chance of mixing for a higher Prandtl number with an increasing Reynolds number, and thus the thermal field becomes more homogeneous due to the enhanced convective effect.

Comparisons of all model predictions show good agreement with the current DNS for all tested Re_τ's and Pr's in the near-wall region. Away from the wall, however, the deviations can be observed more clearly with increasing Pr for $Re_\tau = 180$ and 395. For a higher Pr, ZEROKC overestimates the mean temperature in the outer region, especially more remarkably for lower Re_τ. On the other hand, TWOAKN predicts better for $Pr \leqslant 7.0$, but there still exists an appreciable difference for $Pr = 10.0$. Therefore, further improvement of the modeling for scalar transport is required in consideration of the Pr effect.

5.3. Turbulent Prandtl number

The turbulent Prandtl number Pr_t is shown in Fig. 5. The turbulent Prandtl number Pr_t is defined as the ratio of the momentum eddy diffusivity ν_t to the thermal eddy diffusivity κ_t;

$$Pr_t = \frac{\nu_t}{\kappa_t} = \frac{\overline{u'v'}}{\overline{v'\theta'}}\,\frac{d\overline{\theta}/dy}{d\overline{u}/dy}. \qquad (27)$$

The results obtained by Na and Hanratty (2000) and Kawamura et al. (2004) are also plotted for comparison. Data for $Pr = 0.025$–0.6 in Fig. 5b are obtained from DNS databases at our Web site (http://murasun.me.noda.tus.ac.jp/turbulence/).

Shaw and Hanratty (1977) developed an expression for the conductive sublayer δ_θ connected to the viscous sublayer δ_u and Pr; i.e., $\delta_\theta \approx \delta_u \cdot Pr^{-1/3}$ They indicated that turbulence statistics can be scaled well for different Pr's by using the δ_θ. Certainly, the wall-asymptotic behavior of Pr_t against y/δ_θ can be aligned in the near-wall region as seen in Fig. 5a in the current computational range. The behavior of Pr_t is almost independent for $Pr \leqslant 2.0$. With increasing Pr, the Pr_t increases toward the wall and then stays at a constant value. The wall-asymptotic value stays at about 1.0 for $Pr = 0.20$–2.0, while it increases for smaller and larger Pr's, as gi-

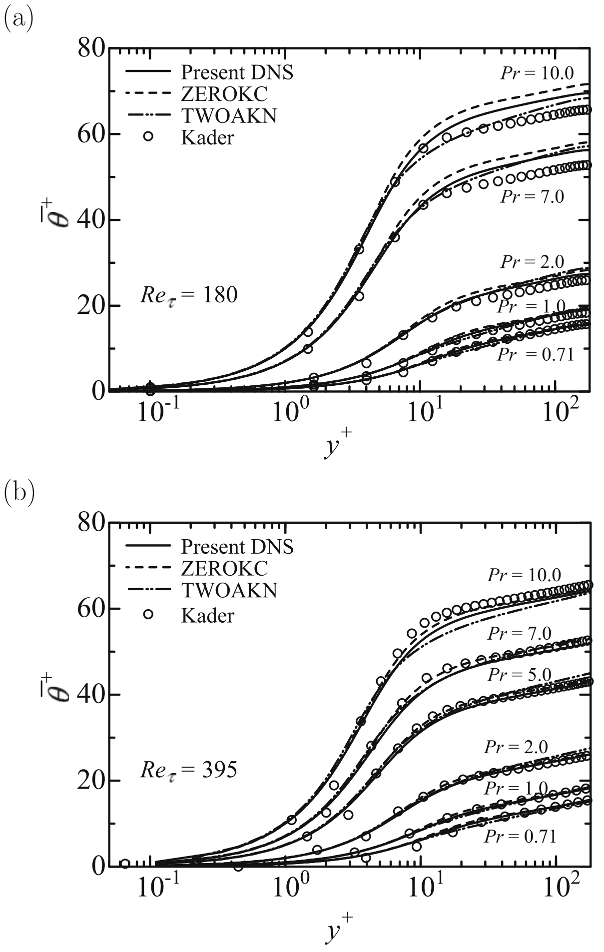

Fig. 4. Profiles of the mean temperature: (a) $Re_\tau = 180$ and (b) $Re_\tau = 395$.

ven in Fig. 5b. The current wall-asymptotic values of Pr_t agree well with those for $Re_\tau = 150$ at $Pr = 1.0$ and 10.0 calculated by Na and Hanratty (2000) and for $Re_\tau = 1020$ at $Pr = 0.71$ (Kawamura et al., 2004). As for the Reynolds-number dependence, its effect is small near the wall for $Pr = 0.71$—10.0, while it is significant for $Pr = 0.025$. In the region within the δ_θ, heat conduction is more dominant than convection, and thus the effect of Re_τ is small. This is why the Reynolds-number dependence is small in the wall-asymptotic behavior of Pr_t.

In the region where y^+ is outside the δ_θ but still $y^+ < 60$, the Pr_t is almost independent of the calculated Re_τ's and Pr's as shown in Fig. 5c. Further away from the wall, the Pr_t stays at a constant value of 0.8 for $Re_\tau = 395$, irrespective of Pr, while it decreases and reaches about 0.65 for $Re_\tau = 180$. In the case of $Re_\tau = 1020$ at $Pr = 0.71$ by Kawamura et al., the Pr_t also stays in a wider region from the wall. This indicates that the higher Re_τ is, the further away from the wall the Pr_t is almost constant. Note that the distributions around the channel center are unstable. This is because $\overline{u'v'}$, $\overline{v'\theta'}$, $d\overline{u}/dy$, $d\overline{\theta}/dy$. in Eq. (27) are all zero at the channel center and its limiting value is difficult to calculate. Therefore, these wiggles can be neglected near the channel center.

5.4. Time scale ratio

The time scale ratio R is shown in Fig. 6. The ratio R is expressed as the ratio of the thermal time scale τ_θ to the momentum one τ_u;

$$R = \frac{\tau_\theta}{\tau_u} = \frac{\overline{\theta'^2}}{2\varepsilon_\theta}\frac{\varepsilon}{k}. \tag{28}$$

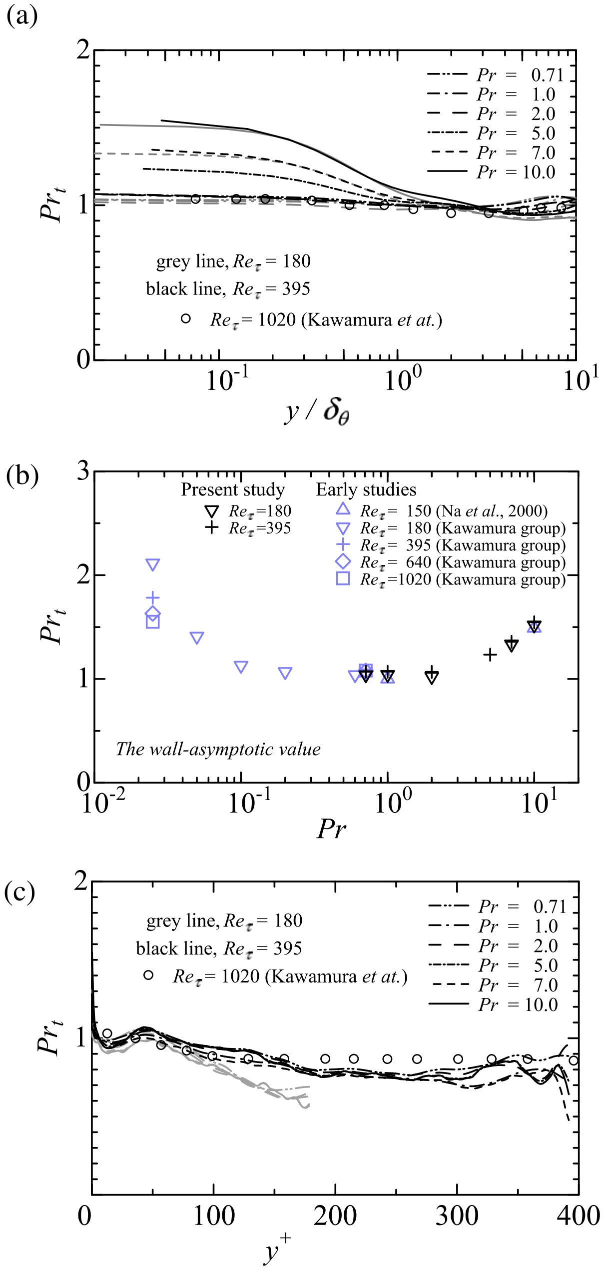

Fig. 5. Profiles of the turbulent Prandtl number: (a) near-wall behavior; (b) wall-asymptotic value and (c) behavior away from the wall.

The profiles of R/Pr are shown in Fig. 6a, where the abscissa is the distance from the wall normalized by δ_θ. The wall-asymptotic value of R is analytically shown as the molecular Prandtl number itself. The profiles of R/Pr given in Fig. 6a indicate that the near-wall limiting value of R certainly corresponds to Pr, and it stays almost constant within the δ_θ for all tested Re_τ's and Pr's. The profiles of R are plotted against y/δ in Fig. 6b. In the case of $Pr = 0.71$, R is almost independent of Re_τ up to $Re_\tau = 1020$ away from the wall. With increasing Pr, the R increases to a constant value of about 1.0, and is also independent of Re_τ up to $Re_\tau = 395$ at $Pr = 10.0$.

5.5. Budget for ε_θ

The ε_θ-budget evaluated from the data for $Re_\tau = 395$ at $Pr = 1.0$ is shown in Fig. 7, where a comparison with existing DNS data for ε-budget by Rodi and Mansour (1993) is made. The individual

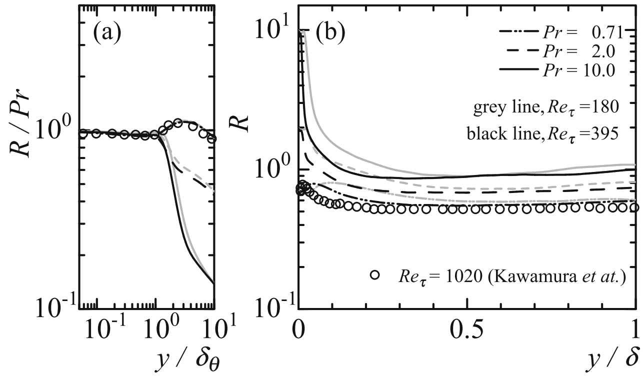

Fig. 6. Profiles of the time scale ratio: (a) near-wall behavior and (b) behavior away from the wall.

terms in the ε-budget are written in the Appendix. The form of the individual terms in Eqs. (5)–(11) are quite similar to those in the transport equation for ε. This indicates that the behavior of the various terms in ε_θ-budget are very similar to the corresponding terms in ε-budget. As expected, there are reasonable overall similarities between the budgets for ε_θ and ε, although differences are noticeable very close to the wall ($y^+ < 5$) between $\gamma_{\varepsilon_\theta}$ and γ_ε. These similarities suggests that a model equation for ε_θ may be constructed in almost the same manner as the one for ε at $Pr \approx 1.0$.

To examine the difference between $\gamma_{\varepsilon_\theta}$ and γ_ε, the near-wall expansions for $\gamma_{\varepsilon_\theta}$ and γ_ε are derived. The dissipation terms in the transport equations for ε_θ and ε are given as:

$$\gamma_{\varepsilon_\theta} = \frac{2}{Pr^2}\overline{\left(\frac{\partial^2\theta'^+}{\partial x_k^+\partial x_m^+}\right)^2}, \tag{29}$$

$$\gamma_\varepsilon = 2\overline{\left(\frac{\partial^2 u_i'^+}{\partial x_k^+\partial x_m^+}\right)^2}. \tag{30}$$

In the wall vicinity, the fluctuations of the velocity and the temperature can be expanded in terms of y^+ as follows:

$$u'^+ = b_1y^+ + c_1y^{+2} + d_1y^{+3} + \cdots \tag{31}$$

$$v'^+ = c_2y^{+2} + d_2y^{+3} + \cdots \tag{32}$$

$$w'^+ = b_3y^+ + c_3y^{+2} + d_3y^{+3} + \cdots \tag{33}$$

$$\theta'^+ = b_\theta y^+ + d_\theta y^{+3} + \cdots \tag{34}$$

Refer to Antonia and Kim (1991) for the absence of b_2 and c_θ. With the use of Eqs. (31)–(34), $\gamma_{\varepsilon_\theta}$ and γ_ε are expressed as:

$$\gamma_{\varepsilon_\theta} = A_{\varepsilon_\theta} + C_{\varepsilon_\theta}y^{+2} + \cdots \tag{35}$$

$$\gamma_\varepsilon = A_\varepsilon + B_\varepsilon y^+ + C_\varepsilon y^{+2} + \cdots \tag{36}$$

$$A_{\varepsilon_\theta} = \frac{4}{Pr^2}\left\{\overline{(b_{\theta,1})^2} + \overline{(b_{\theta,3})^2}\right\}, \tag{37}$$

$$A_\varepsilon = \frac{4}{Re_\tau}\left\{2\overline{c_1^2} + 2\overline{c_2^2} + 2\overline{c_3^2} + \overline{(b_{1,1})^2} + \overline{(b_{1,3})^2} + \overline{(b_{3,1})^2} + \overline{(b_{3,3})^2}\right\}, \tag{38}$$

$$\begin{aligned} B_\varepsilon = {} & \frac{48}{Re_\tau}\left\{\overline{c_1d_1} + \overline{c_2d_2} + \overline{c_3d_3}\right\} \\ & + \frac{16}{Re_\tau}\left\{\overline{b_{1,1}c_{1,1}} + \overline{b_{1,3}c_{1,3}} + \overline{b_{3,1}c_{3,1}} + \overline{b_{3,3}c_{3,3}}\right\}, \end{aligned} \tag{39}$$

$$\begin{aligned} C_{\varepsilon_\theta} = {} & \frac{2}{Pr^2}\left\{\overline{(b_{\theta,11})^2} + \overline{(b_{\theta,33})^2} + 2\overline{(b_{\theta,13})^2}\right\} \\ & + \frac{2}{Pr^2}\left\{36\overline{d_\theta^2} + 12\overline{b_{\theta,1}d_{\theta,1}} + 12\overline{b_{\theta,3}d_{\theta,3}}\right\}, \end{aligned} \tag{40}$$

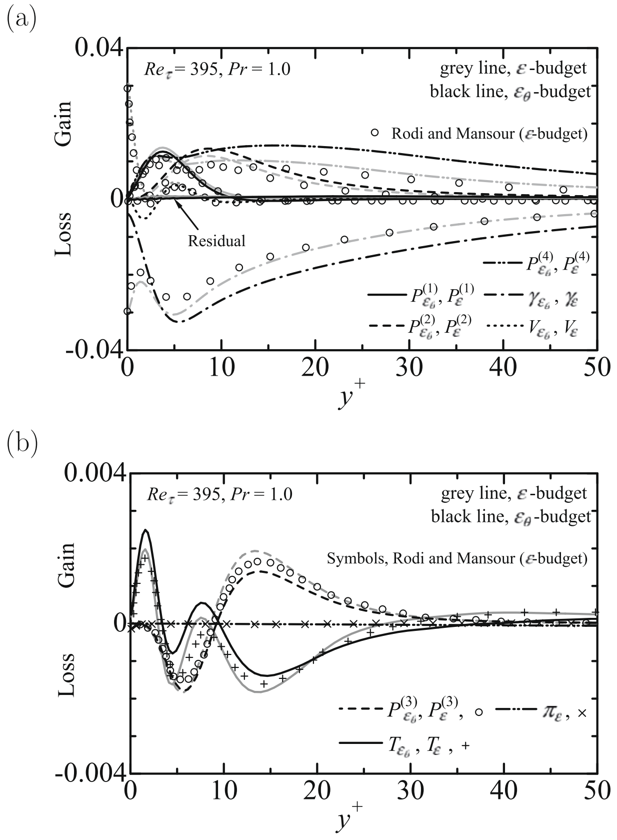

Fig. 7. The individual terms in the transport equations for ε_θ and ε with $Re_\tau = 395$ at $Pr = 1.0$: (a) relatively large terms and (b) small terms.

$$\begin{aligned} C_\varepsilon = {} & \frac{2}{Re_\tau}\left\{\overline{(b_{1,11})^2} + \overline{(b_{1,33})^2} + \overline{(b_{3,11})^2} + \overline{(b_{3,33})^2}\right\} \\ & + \frac{16}{Re_\tau}\left\{\overline{(c_{1,1})^2} + \overline{(c_{1,3})^2} + \overline{(c_{2,1})^2} + \overline{(c_{2,3})^2} + \overline{(c_{3,1})^2} + \overline{(c_{3,3})^2}\right\} \\ & + \frac{24}{Re_\tau}\left\{3\overline{d_1^2} + 3\overline{d_2^2} + 3\overline{d_3^2} + 4\overline{c_1e_1} + 4\overline{c_2e_2} + 4\overline{c_3e_3}\right\} \\ & + \frac{24}{Re_\tau}\left\{\overline{b_{1,1}d_{1,1}} + \overline{b_{1,3}d_{1,3}} + \overline{b_{3,1}d_{3,1}} + \overline{b_{3,3}d_{3,3}}\right\} \\ & + \frac{8}{Re_\tau}\left\{\overline{(b_{1,13})^2} + \overline{(b_{3,13})^2}\right\}, \end{aligned} \tag{41}$$

where $\alpha_{,i} = \partial\alpha/\partial x_i$ and $\alpha_{,ij} = \partial^2\alpha/\partial x_i\partial x_j$. It should be noted that B_{ε_θ} in the expansion of $\gamma_{\varepsilon_\theta}$ becomes zero. This is confirmed in the current DNS as seen in Fig. 7a. The coefficients of y^{+2} in Eqs. (35) and (36); i.e., C_{ε_θ} and C_ε are composed mostly with positive terms. Thus one can expect that C_{ε_θ} and C_ε are positive, although it cannot be proven exactly. Indeed, the positivity of C_{ε_θ} causes the remarkable increase in the absolute value of $\gamma_{\varepsilon_\theta}$ near the wall as seen in Fig. 7a. On the other hand, the absolute value of γ_ε decreases in the wall vicinity (see Fig. 7a). This results from the negativity of B_ε. This causes the notable difference between $\gamma_{\varepsilon_\theta}$ and γ_ε observed in their near-wall limiting behaviors.

The budget for ε_θ with $Re_\tau = 180$ and 395 at $Pr = 7.0$ is shown in Fig. 8. Abe et al. (2008) pointed out that the Reynolds-number dependence of the budget for ε_θ exhibits the same trends as the one for ε in the range of $Re_\tau = 180$–640 at $Pr = 0.71$. They also indicated that the terms of $P^{(1)}_{\varepsilon_\theta}$, $P^{(2)}_{\varepsilon_\theta}$ and $P^{(4)}_{\varepsilon_\theta}$ depend on Re_τ especially close to the wall, while $P^{(3)}_{\varepsilon_\theta}$ is independent of Re_τ at $Pr = 0.71$. Even for higher Pr, the Re dependence of these production terms holds the trends; i.e., there are negligible Re effects on

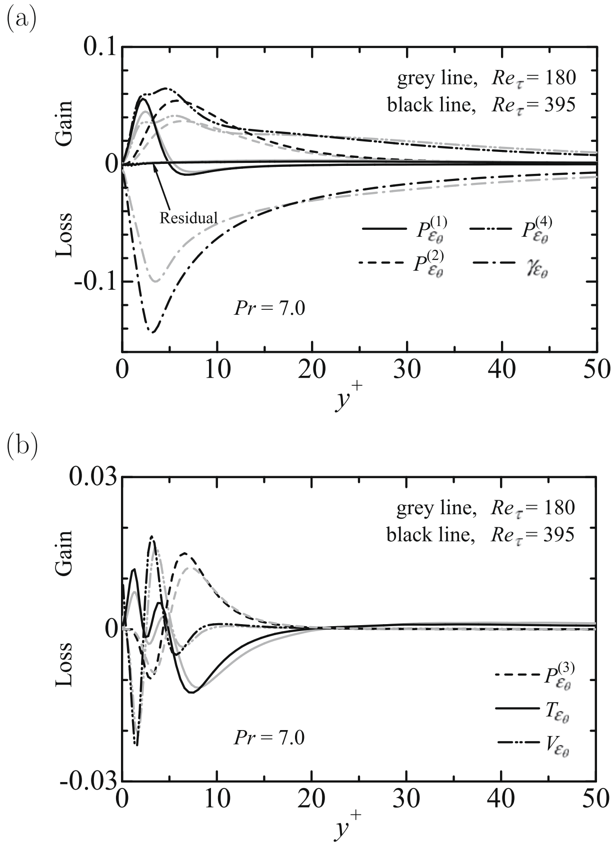

Fig. 8. The individual terms in the transport equation for ε_θ with $Re_\tau = 180$ and 395 at $Pr = 7.0$: (a) relatively large terms and (b) small terms.

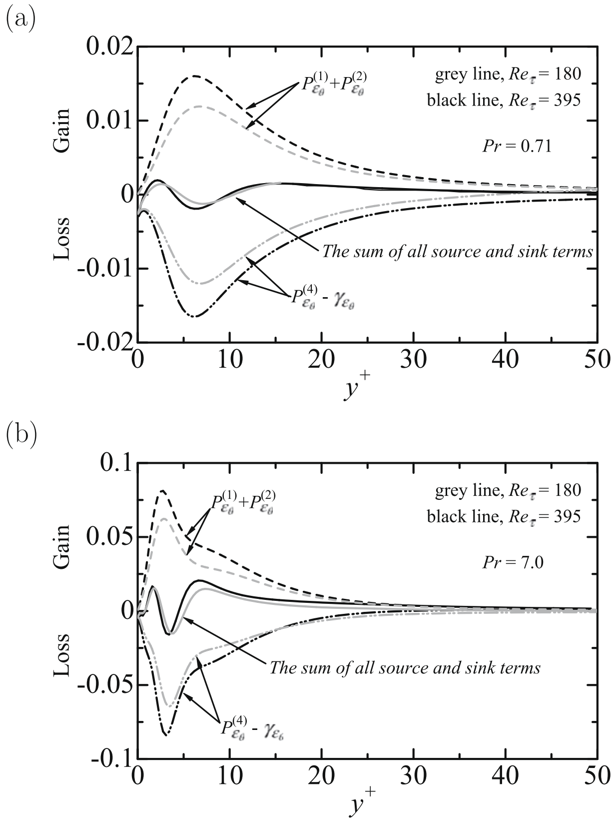

Fig. 9. Profiles of the sums of the terms in ε_θ-budget: (a) $Pr = 0.71$ and (b) $Pr = 7.0$.

the term of $P^{(3)}_{\varepsilon_\theta}$ and the other production terms change appreciably with increasing Re_τ for $Pr = 7.0$, which is consistent with the *Re* effect on the $\gamma_{\varepsilon_\theta}$.

Distributions of the sum of the several terms in the budget for ε_θ are shown in Fig. 9. Rodi and Mansour (1993) examined the budget for ε and indicated that the individual and divided sums of the terms are greatly influenced by Re_τ in the near-wall region, while the sum of all source and sink terms is less in the ε-budget. In the case of ε_θ-budget also, $P^{(1)}_{\varepsilon_\theta} + P^{(2)}_{\varepsilon_\theta} + P^{(3)}_{\varepsilon_\theta} + P^{(4)}_{\varepsilon_\theta} - \gamma_{\varepsilon_\theta}$ is almost independent of Re_τ for $Pr = 0.71$ and 7.0 as given in Fig. 9a and b. This may be useful for the development of the turbulence modeling of ε_θ-equation. Rodi's further investigations of divided sums of $P^{(1)}_{\varepsilon} + P^{(2)}_{\varepsilon}$ and $P^{(4)}_{\varepsilon} - \gamma_\varepsilon$ in the ε-budget indicate there is no noticeable *Re* dependence on either group of the terms away from the wall, whereas both groups increase with increasing Re_τ close to the wall. Likewise in the ε_θ-budget, the corresponding terms show a similar tendency; i.e., $P^{(1)}_{\varepsilon_\theta} + P^{(2)}_{\varepsilon_\theta}$ and $P^{(4)}_{\varepsilon_\theta} - \gamma_{\varepsilon_\theta}$ are almost independent of Re_τ away from the wall, while they go up somewhat for higher Re_τ in the near-wall region at $Pr = 0.71$ and 7.0 (see Fig. 9b).

Critical assessments of the modeling of the transport equation of $\varepsilon_\theta(\widetilde{\varepsilon_\theta})$ are made with a focus on the effect of *Pr*. Four models (Nagano et al., 1991 (NTT), Abe et al., 1995 (AKN), Wakao and Kawamura, 1996 (WK) and Hattori and Nagano, 1998 (HN)) are tested against current DNS data for $Re_\tau = 395$ at $Pr = 0.71$ and 7.0. For a proper comparison, all turbulence quantities, except for ε_θ, are directly given from the current DNS data. The modeled equation for ε_θ and the employed model constants and functions can be found in the above-cited papers.

The model predictions of ε_θ for $Re_\tau = 395$ at $Pr = 0.71$ and 7.0 are shown in Fig. 10. Away from the wall, the agreement is good in the four tested models for $Pr = 0.71$. Close to the wall ($y^+ < 20$), there are discernible differences between the DNS and the model predictions. WK and HN yield the better predictions among the tested models. With increasing *Pr*, all tested models deviate remarkably from the DNS data in the near-wall region (see Fig. 10b). The near-wall expansion for ε_θ indicates $\partial\varepsilon_\theta/\partial y = 0$ at the wall. WK, NTT and HN models fulfill this property at $Pr = 0.71$, while they fail at $Pr = 7.0$. The AKN model yields the best prediction among the three tested models at $Pr = 7.0$.

The model predictions of the sum of all source and sink terms $P^{(1)}_{\varepsilon_\theta} + P^{(2)}_{\varepsilon_\theta} + P^{(3)}_{\varepsilon_\theta} + P^{(4)}_{\varepsilon_\theta} - \gamma_{\varepsilon_\theta}$ are shown in Fig. 11. NTT, WK and AKN do not reproduce the correct near-wall behavior for the tested Re_τ's and *Pr*'s. HN has advantages in the modeling of the sum for $Re_\tau = 395$ at $Pr = 0.71$ as seen in Fig. 11a, whereas it has difficulty in predicting higher *Pr* (see Fig. 11b).

The production term of $P^{(3)}_{\varepsilon_\theta}$ given by the models is shown in Fig. 12. The relatively small production term $P^{(3)}_{\varepsilon_\theta}$ is of the same order of magnitude as T_{ε_θ} and $P^{(1)}_{\varepsilon_\theta} + P^{(2)}_{\varepsilon_\theta} + P^{(3)}_{\varepsilon_\theta} + P^{(4)}_{\varepsilon_\theta} - \gamma_{\varepsilon_\theta}$. Therefore, the modeling of the individual term is a key to developing the modeling for the rigorous ε_θ-equation. In the case of $Pr = 0.71$, WK and HN model predictions are in good agreement with DNS. However, with increasing *Pr*, these models overestimate and their deviations become more significant.

To summarize the model assessment, the HN model gives more reasonable results than the others for the modeling of ε_θ in near-wall region with $Pr \approx 1$. However, with increasing *Pr*, none of the existing models can predict the correct near-wall behavior of the individual and the sums of the terms in ε_θ-budget.

5.6. Budgets for $\overline{u'_i\theta'}$ and $\varepsilon_{i\theta}$

The budgets for the streamwise and the wall-normal turbulent heat flux given by Eqs. (13)–(17) are shown in Figs. 13 and 14, respectively. It is well known that the dissipation $\varepsilon_{i\theta}$ is negligible

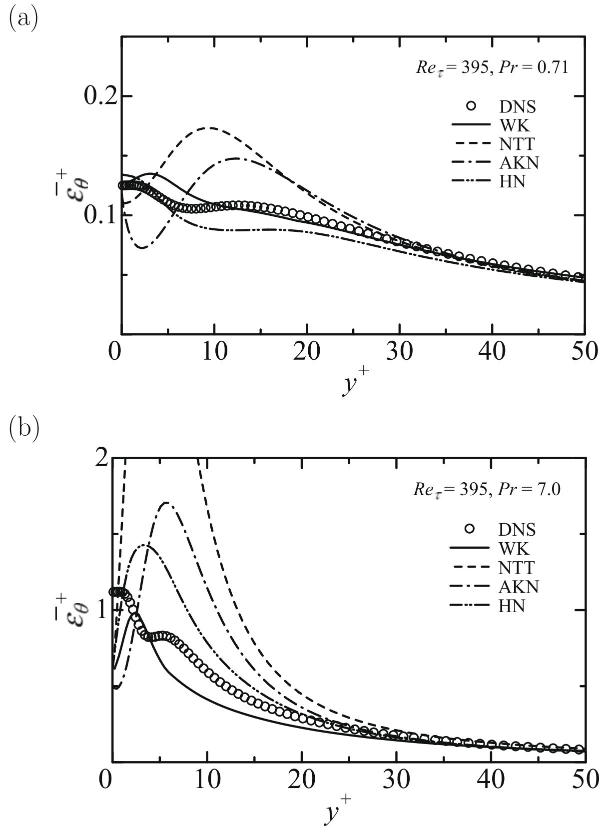

Fig. 10. Comparisons of the existing heat transfer models with DNS for ε_θ: (a) $Pr = 0.71$ and (b) $Pr = 7.0$.

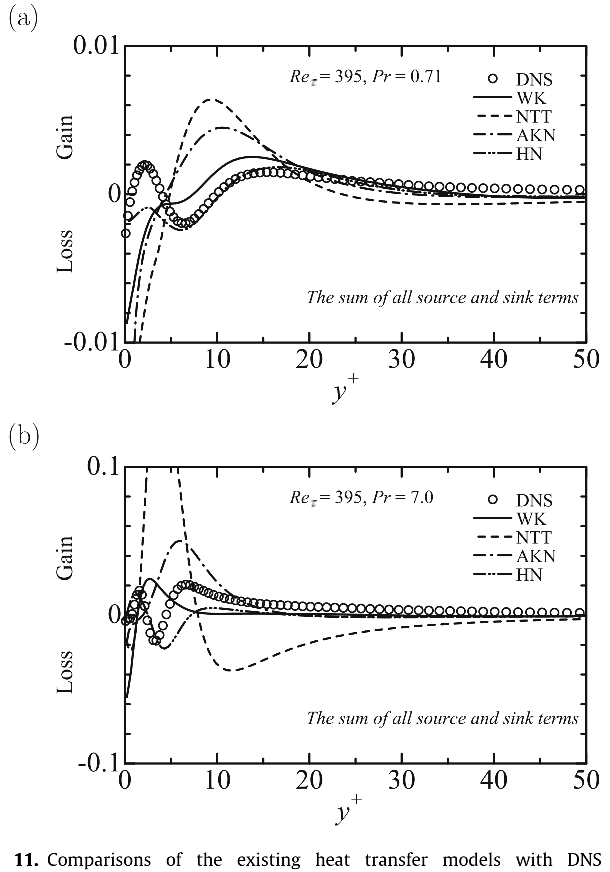

Fig. 11. Comparisons of the existing heat transfer models with DNS for $P^{(1)}_{\varepsilon_\theta} + P^{(2)}_{\varepsilon_\theta} + P^{(3)}_{\varepsilon_\theta} + P^{(4)}_{\varepsilon_\theta} - \gamma_{\varepsilon_\theta}$: (a) $Pr = 0.71$ and (b) $Pr = 7.0$.

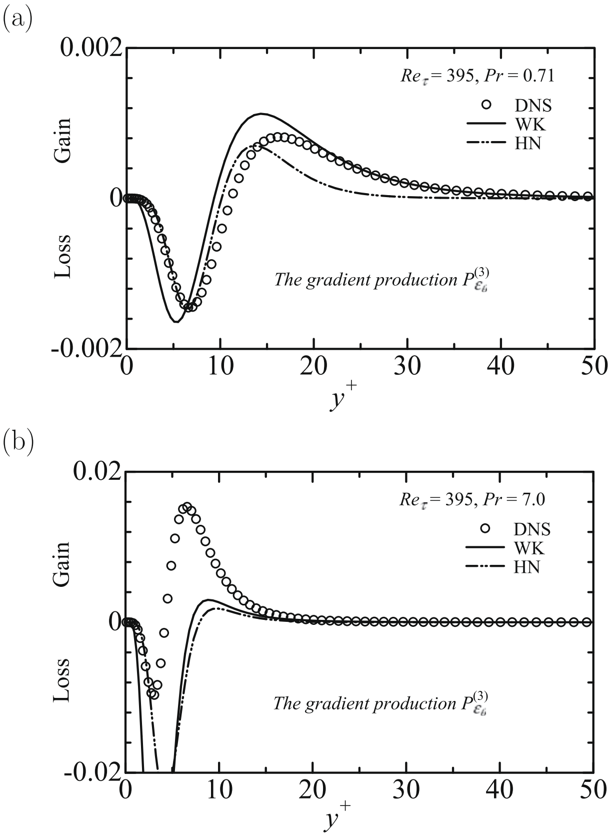

Fig. 12. Comparisons of the existing heat transfer models with DNS for $P^{(3)}_{\varepsilon_\theta}$: (a) $Pr = 0.71$ and (b) $Pr = 7.0$.

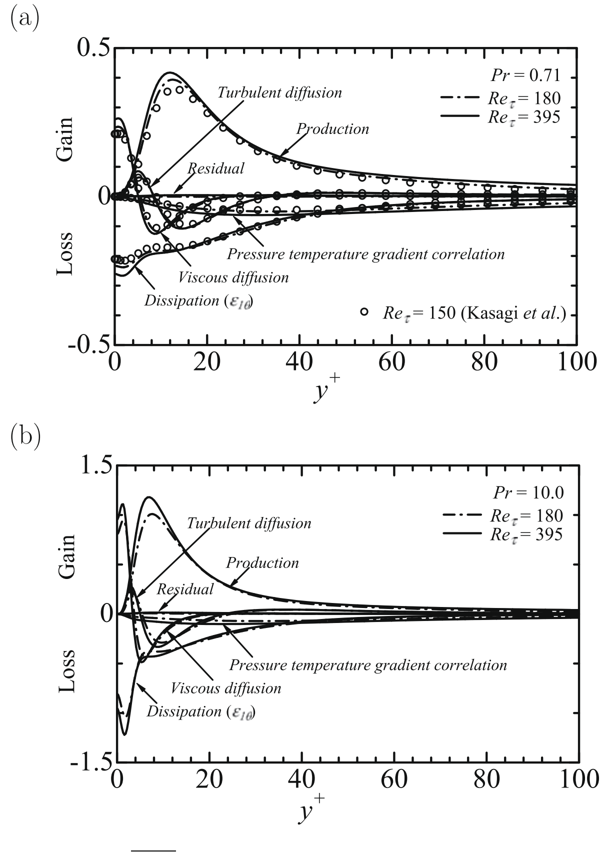

Fig. 13. Budget for $\overline{u'^+\theta'^+}$ with $Re_\tau = 180$ and 395: (a) $Pr = 0.71$ and (b) $Pr = 10.0$.

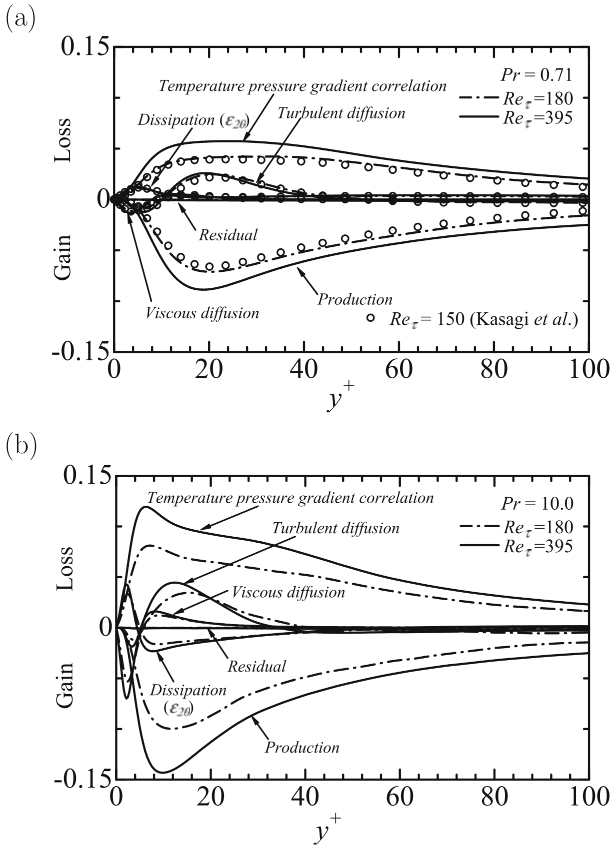

Fig. 14. Budget for $\overline{v'^+\theta'^+}$ with $Re_\tau = 180$ and 395: (a) $Pr = 0.71$ and (b) $Pr = 10.0$.

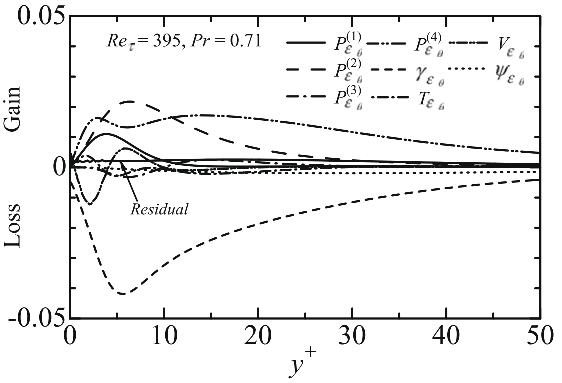

Fig. 15. Budget for $\varepsilon_{1\theta}$ with $Re_\tau = 395$ at $Pr = 0.71$.

in the case of fluids with $Pr \geqslant 1.0$ because of the isotropy in the dissipation scale. In the case of the budget for $\overline{u'^+\theta'^+}$, $\varepsilon_{1\theta}$ is large over the channel section for $Pr = 0.71$ as seen in Fig. 13a. This is because, in the current thermal boundary condition, the correlation between u' and θ' is very high. The dissipation $\varepsilon_{1\theta}$ is balanced with the sum of the production $P_{1\theta}$ and the temperature pressure gradient correlation $\pi_{1\theta}$ terms away from the wall, and with the viscous term $V_{1\theta}$ at the wall. With increasing Pr, $\varepsilon_{1\theta}$ and $V_{1\theta}$ becomes more effective in the viscous sublayer as seen in Fig. 13b.

In the case of the budget for $\overline{v'^+\theta'^+}$ (see Fig. 14a), the dissipation rate $\varepsilon_{2\theta}$ is certainly small away from the wall. In the near-wall vicinity, on the other hand, it is comparable to the dominative production and temperature pressure gradient correlation terms for $Pr = 0.71$. For higher Pr, the $\varepsilon_{2\theta}$ contributes more significantly in the range up to $y^+ = 40$ as seen in Fig. 14b. This suggests that in the modeling of the dissipation rate of the turbulent heat flux the $\varepsilon_{i\theta}$ should not be ignored for $Pr > 1$ in the near-wall region.

The terms in the budgets for the dissipation rate of the streamwise and the wall-normal turbulent heat flux are shown in Figs. 15 and 16, respectively. For the $\varepsilon_{1\theta}$-budget in Fig. 15, the $P^{(4)}_{\varepsilon_{1\theta}}$ and $\gamma_{\varepsilon_{1\theta}}$ are the major contributors to $\varepsilon_{1\theta}$ away from the wall, where the $\psi_{\varepsilon_{1\theta}}$ is small, but always lies in the loss side. Down to the wall, $P^{(4)}_{\varepsilon_{1\theta}}$ still remains large, but relatively small compared to $P^{(1)}_{\varepsilon_{1\theta}}$ and $P^{(2)}_{\varepsilon_{1\theta}}$ in the near-wall region. The $P^{(1)}_{\varepsilon_{1\theta}}$ and $P^{(2)}_{\varepsilon_{1\theta}}$ are of the same order of magnitude as the $P^{(4)}_{\varepsilon_{1\theta}}$ in the region of $y^+ < 20$, while the $P^{(3)}_{\varepsilon_{1\theta}}$ is relatively small over the channel section. Both diffusion terms T_{ε_θ} and V_{ε_θ} are appreciable only in the region of $y^+ < 10$. Overall, the $\varepsilon_{1\theta}$-budget is similar to ε_θ-budget for $Pr = 0.71$. This is due to the strong correlation between u' and θ' for $Pr \approx 1.0$.s.

For the $\varepsilon_{2\theta}$-budget in Fig. 16, the temperature gradient correlation (Eq. (25)) can be split into two terms as:

$$-\left(1+\frac{1}{Pr}\right)\overline{\frac{\partial\theta'^+}{\partial x_j^+}\frac{\partial^2 p'^+}{\partial x_2^+\partial x_j^+}} = -\left(1+\frac{1}{Pr}\right)\frac{\partial}{\partial x_2^+}\left(\overline{\frac{\partial p'^+}{\partial x_j^+}\frac{\partial\theta'^+}{\partial x_j^+}}\right) + \left(1+\frac{1}{Pr}\right)\overline{\frac{\partial p'^+}{\partial x_j^+}\frac{\partial^2\theta'^+}{\partial x_2^+\partial x_j^+}}, \tag{42}$$

which are called the pressure diffusion $\pi_{\varepsilon_{2\theta}}$ and the pressure gradient correlation $\phi_{\varepsilon_{2\theta}}$ terms, respectively. Note that $\pi_{\varepsilon_{2\theta}}$ appears in $\varepsilon_{2\theta}$ budget, but not in $\varepsilon_{1\theta}$. As shown in Fig. 16, the $\phi_{\varepsilon_{2\theta}}$ balances with $P^{(1)}_{\varepsilon_{1\theta}}$ and $\gamma_{\varepsilon_{2\theta}}$ away from the wall. The pressure diffusion term $\pi_{\varepsilon_{2\theta}}$ becomes even more dominant in the wall vicinity.

6. Conclusions

In the current study, by employing high spatial resolution comparable to the Batchelor length scale, we performed a series of DNS of turbulent channel flow with a passive scalar field for moderate Reynolds and Prandtl numbers. We investigated the effects of the Reynolds and Prandtl numbers on turbulence statistics such as turbulent Prandtl number, time scale ratio, and budget for the dissipation rate of the temperature variance. Ranges of Reynolds and Prandtl numbers were $Re_\tau = 180$ and 395, $Pr = 0.71$—10.0.

Based on the results, the performance of Kader's empirical equation was discussed. It agreed sufficiently well with the current data, but the deviation increased with the increase in the Prandtl number. The behavior of the turbulent Prandtl number Pr_t was also examined. The near-wall-asymptotic value of Pr_t stayed almost constant between $Pr = 0.20$—2.0 and increased for both decreasing and increasing Prandtl numbers. Time scale ratio R was equal to the molecular Prandtl number in the near-wall region as predicted theoretically. This region of $R = Pr$ can be well scaled by the thickness of the conductive sublayer, independent of Reynolds and Prandtl numbers.

Budgets for ε_θ and ε were obtained with a high accuracy.

The wall-asymptotic behaviors of $\gamma_{\varepsilon_\theta}$ and γ_ε were examined using near-wall expansions. A notable difference was observed in the near-wall limiting behaviors of $\gamma_{\varepsilon_\theta}$ and γ_ε. This was caused by the difference in the expansions' coefficients of $\gamma_{\varepsilon_\theta}$ and γ_ε; i.e., the positivity of C_{ε_θ} and the negativity of B_ε. Reynolds and Prandtl number dependencies were investigated in the individual and sums of the terms in ε_θ-budget. The sum of all source and sink terms was almost independent of Re_τ for $Pr = 0.71$ and 7.0. The sums $P^{(1)}_{\varepsilon_\theta} + P^{(2)}_{\varepsilon_\theta}$ and $P^{(4)}_{\varepsilon_\theta} - \gamma_{\varepsilon_\theta}$ increased in the region of $y^+ < 20$ with an increase in Re_τ. The Reynolds-number dependence on the individual terms showed a similar tendency between $Pr = 0.71$ and 7.0; i.e., $P^{(1)}_{\varepsilon_\theta}$, $P^{(2)}_{\varepsilon_\theta}$ and $P^{(4)}_{\varepsilon_\theta}$ showed a noticeable Re_τ effect close to the wall, while $P^{(3)}_{\varepsilon_\theta}$ was almost independent of Re_τ for $Pr = 0.71$—7.0. The budgets for $\varepsilon_{1\theta}$ and $\varepsilon_{2\theta}$ were also obtained. The

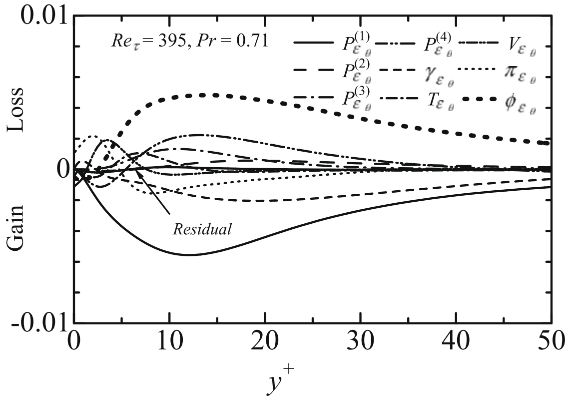

Fig. 16. Budget for $\varepsilon_{2\theta}$ with $Re_\tau = 395$ at $Pr = 0.71$.

$\varepsilon_{1\theta}$-budget was similar to ε_θ-budget with $Pr = 0.71$ due to the strong correlation between u' and θ'.

Assessments of the existing modeled equation for ε_θ revealed that most models deviated with the current DNS data more appreciably with the increasing *Pr*. All the model predictions of ε_θ showed remarkable differences from the DNS in the near-wall region with increasing *Pr* up to 7.0. The model of Hattori and Nagano (1998) yielded the best prediction of the sum of all the source and sink terms at $Pr = 0.71$. However with an increase in *Pr*, the model did not reproduce the correct near-wall behavior. The disagreements were due to the lack of information about high *Pr*. For example, the model constants in the assessed models were determined on the basis of the assumptions of constant $Pr_t (= 0.9)$ and $R (= 0.5)$. However, recent DNS reveals that Pr_t and *R* vary with *y* and show the sharp increases in the near-wall region. Therefore, the correct information should be incorporated in modeling of the turbulent heat transfer with more attention for a wider range of *Pr* effect. The current statistical DNS databases are available from the current research groups' Web site (http://murasun.me.noda.tus.ac.jp/db/index.html).

Acknowledgements

The current results were obtained using supercomputing resources at the Information Synergy Center (currently: Cyberscience Center), Tohoku University. This work was conducted at the Research Center for Holistic Computational Science (Holcs), which is supported by the Ministry of Education, Culture, Sports, Science and Technology – Japan (MEXT).

Appendix

The exact transport equation for ε derived from the Navier–Stokes equation can be written as follows:

$$\frac{D\varepsilon}{Dt} = P^{(1)}_\varepsilon + P^{(2)}_\varepsilon + P^{(3)}_\varepsilon + P^{(4)}_\varepsilon + T_\varepsilon + V_\varepsilon + \pi_\varepsilon - \gamma_\varepsilon. \tag{43}$$

Mixed production:

$$P^{(1)}_\varepsilon = -2\nu \overline{\frac{\partial u'_i}{\partial x_k}\frac{\partial u'_j}{\partial x_k}}\frac{\partial \overline{u_i}}{\partial x_j}. \tag{44}$$

Production by mean velocity gradient:

$$P^{(2)}_\varepsilon = -2\nu \overline{\frac{\partial u'_i}{\partial x_j}\frac{\partial u'_i}{\partial x_k}}\frac{\partial \overline{u_j}}{\partial x_k}. \tag{45}$$

Gradient production:

$$P^{(3)}_\varepsilon = -2\nu \overline{u'_j \frac{\partial u'_i}{\partial x_k}}\frac{\partial^2 \overline{u_i}}{\partial x_j \partial x_k}. \tag{46}$$

Turbulent production:

$$P^{(4)}_\varepsilon = -2\nu \overline{\frac{\partial u'_i}{\partial x_k}\frac{\partial u'_j}{\partial x_k}\frac{\partial u'_i}{\partial x_j}}. \tag{47}$$

Turbulent diffusion:

$$T_\varepsilon = -\nu \frac{\partial}{\partial x_j}\left(\overline{u'_j \frac{\partial u'_i}{\partial x_k}\frac{\partial u'_i}{\partial x_k}}\right). \tag{48}$$

Viscous diffusion:

$$V_\varepsilon = \nu \frac{\partial^2 \varepsilon}{\partial x_j \partial x_j} = \nu^2 \frac{\partial^2}{\partial x_j^2}\left(\overline{\frac{\partial u_i}{\partial x_k}\frac{\partial u_i}{\partial x_k}}\right). \tag{49}$$

Pressure diffusion:

$$\pi_\varepsilon = -\nu \frac{2}{\rho}\frac{\partial}{\partial x_k}\left(\overline{\frac{\partial p}{\partial x_j}\frac{\partial u_k}{\partial x_j}}\right). \tag{50}$$

Dissipation:

$$\gamma_\varepsilon = 2\nu^2 \left(\overline{\frac{\partial^2 u'_i}{\partial x_k \partial x_j}\frac{\partial^2 u'_i}{\partial x_k \partial x_j}}\right). \tag{51}$$

In Section 5.5, the individual terms normalized by u_τ and ν are compared with the corresponding terms in ε_θ-budget.

References

Abe, H., Kawamura, H., 2002. A study of turbulence thermal structure in a channel flow through DNS up to $Re_\tau = 640$ with $Pr = 0.025$ and 0.71. In: Proc. of Ninth European Turbulence Conference, pp. 399–402.

Abe, K., Kondoh, T., Nagano, Y., 1995. A new turbulence model for predicting fluid flow and heat transfer in separating and reattaching flow – II. Thermal field calculations. Int. J. Heat Mass Transfer 38, 1467–1481.

Abe, H., Kawamura, H., Matsuo, Y., 2004. Surface heat-flux fluctuations in a turbulent channel flow up to $Re_\tau = 1020$ with $Pr = 0.025$ and 0.71. Int. J. Heat Fluid Flow 25, 404–419.

Abe, H., Antonia, R.A., Kawamura, H., 2008. Transport equations for the enstrophy and scalar dissipation rate in a turbulent channel flow. In: Proc. Seventh Int. Symp. on Engineering Turbulence Modelling and Measurements, vol. 3, pp. 750–755.

Antonia, R.A., Kim, J., 1991. Turbulent Prandtl number in the near wall region of a turbulent channel flow. Int. J. Heat Mass Transfer 34, 1905–1908.

Hattori, H., Nagano, Y., 1998. Rigorous formulation of two-equation heat transfer model of turbulence using direct simulations. Numer. Heat Transfer Part B: Fund. 33, 153–180.

Kader, B.A., 1981. Temperature and concentration profiles in fully turbulent boundary layers. Int. J. Heat Mass Transfer 24, 1541–1544.

Kasagi, N., Tomita, Y., Kuroda, A., 1992. A direct numerical simulation for passive scalar field in a turbulent channel flow. ASME J. of Heat Transfer 114, 598–606.

Kawamura, H., Ohsaka, K., Abe, H., Yamamoto, K., 1998. DNS of turbulent heat transfer in a channel flow with low to medium-high Prandtl number fluid. Int. J. Heat Fluid Flow 19, 482–491.

Kawamura, H., Abe, H., Matsuo, Y., 1999. DNS of turbulent heat transfer in a channel flow with respect to Reynolds and Prandtl number effects. Int. J. Heat Fluid Flow 20, 196–207.

Kawamura, H., Abe, H., Shingai, K., 2000. DNS of turbulence and heat transport in a channel flow with different Reynolds and Prandtl numbers and boundary conditions. In: Proc. Third Int. Symp. on Turbulence, Heat and Mass Transfer, pp. 15–32.

Kawamura, H., Abe, H., Matsuo, Y., 2004. Very large-scale structures observed in DNS of turbulent channel flow with passive scalar transport. CD-ROM of 15th Australasian Fluid Mechanics Conference.

Kays, W., Crawford, M., 2004. Convective Heat and Mass Transfer, second ed. MacGraw-Hill.

Kida, S., Yanase, S., 1999. Dynamics of Turbulence (in Japanese). Asakura Shoten Co. Ltd..

Kim, J., Moin, P., 1989. Transport of passive scalars in a turbulent channel flow. Turb. Shear Flow 6, 85–96.

Lyons, S.L., Hanratty, T.J., Mclaughlin, J.B., 1991. Direct numerical simulation of passive scalar heat transfer in a turbulent channel flow. Int. J. Heat Mass Transfer 39, 1149–1161.

Na, Y., Hanratty, T.J., 2000. Limiting behavior of turbulent scalar transport close to the wall. Int. J. Heat Mass transfer 43, 1749–1758.

Nagano, Y., Tagawa, M., Tsuji, T., 1991. An improved two-equation heat transfer model for wall turbulent shear flows. In: Proc. ASME/JSME Thermal Engineering Joint Conf., vol. 3, pp. 233–240.

Rodi, W., Mansour, N.N., 1993. Low Reynolds number k–ε modelling with the aid of direct simulation data. J. Fluid Mech. 250, 509–529.

Shaw, D.A., Hanratty, T.J., 1977. Turbulent mass transfer rates to a wall for large Schmidt numbers. AIChE J. 23, 28–37.
Tennekes, H., Lumley, J.L., 1972. A First Course in Turbulence. The MIT Press.
Tiselj, I., Pogrebnyak, E., Li, C., Mosyak, A., Hetsroni, G., 2001. Effect of wall boundary condition on scalar transfer in a fully developed turbulent flume. Phys. Fluids 13, 1028–1039.
Wakao, Y., Kawamura, H., 1996. Modelling of scalar transport in a turbulent channel flow consistent with the linearity principle. Trans. Jpn. Soc. Mech. Eng. B 62, 3934–3942.